Lundgren, P., Nikkhoo, M., Samsonov, S. V., Milillo, P., Gil-Cruz, F., Lazo, J. (2017): Source model for the Copahue volcano magma plumbing system constrained by InSAR surface deformation observations. - *Journal of Geophysical Research*, *122*, 7, pp. 5729—5747.

DOI: http://doi.org/10.1002/2017JB014368

AGU PUBLICATIONS

JGR

Journal of Geophysical Research: Solid Earth

RESEARCH ARTICLE
10.1002/2017JB014368

Key Points:
- InSAR time series reveal an asymmetric deformation pattern concurrent with eruptive activity
- Two nonstandard sources are required: shallow summit and a deeper conduit system plunging into the caldera
- Compared to seismicity, we suggest that the summit connects via the deep source to the central caldera

Supporting Information:
- Supporting Information S1
- Table S1
- Table S2
- Table S3

Correspondence to:
P. Lundgren,
paul.lundgren@jpl.nasa.gov

Citation:
Lundgren, P., M. Nikkhoo, S. V. Samsonov, P. Milillo, F. Gil-Cruz, and J. Lazo (2017), Source model for the Copahue volcano magma plumbing system constrained by InSAR surface deformation observations, *J. Geophys. Res. Solid Earth*, *122*, 5729–5747, doi:10.1002/2017JB014368.

Received 25 APR 2017
Accepted 19 JUN 2017
Accepted article online 21 JUN 2017
Published online 20 JUL 2017

Source model for the Copahue volcano magma plumbing system constrained by InSAR surface deformation observations

Paul Lundgren[1], Mehdi Nikkhoo[2], Sergey V. Samsonov[3], Pietro Milillo[1], Fernando Gil-Cruz[4], and Jonathan Lazo[4]

[1]Jet Propulsion Laboratory, California Institute of Technology, Pasadena, California, USA, [2]GFZ German Research Centre for Geosciences, Potsdam, Germany, [3]Canada Centre for Mapping and Earth Observation, Natural Resources Canada, Ottawa, Ontario, Canada, [4]Observatorio Vulcanológico de los Andes del Sur, Servicio Nacional de Geología y Minería, Temuco, Chile

Abstract Copahue volcano straddling the edge of the Agrio-Caviahue caldera along the Chile-Argentina border in the southern Andes has been in unrest since inflation began in late 2011. We constrain Copahue's source models with satellite and airborne interferometric synthetic aperture radar (InSAR) deformation observations. InSAR time series from descending track RADARSAT-2 and COSMO-SkyMed data span the entire inflation period from 2011 to 2016, with their initially high rates of 12 and 15 cm/yr, respectively, slowing only slightly despite ongoing small eruptions through 2016. InSAR ascending and descending track time series for the 2013–2016 time period constrain a two-source compound dislocation model, with a rate of volume increase of 13×10^6 m^3/yr. They consist of a shallow, near-vertical, elongated source centered at 2.5 km beneath the summit and a deeper, shallowly plunging source centered at 7 km depth connecting the shallow source to the deeper caldera. The deeper source is located directly beneath the volcano tectonic seismicity with the lower bounds of the seismicity parallel to the plunge of the deep source. InSAR time series also show normal fault offsets on the NE flank Copahue faults. Coulomb stress change calculations for right-lateral strike slip (RLSS), thrust, and normal receiver faults show positive values in the north caldera for both RLSS and normal faults, suggesting that northward trending seismicity and Copahue fault motion within the caldera are caused by the modeled sources. Together, the InSAR-constrained source model and the seismicity suggest a deep conduit or transfer zone where magma moves from the central caldera to Copahue's upper edifice.

Plain Language Summary Copahue volcano straddling the edge of the Agrio-Caviahue caldera along the Chile-Argentina border in the southern Andes has been in unrest since inflation began in late 2011. Its asymmetric deformation pattern extending into the caldera observed by radar interferometry suggests a complex magma plumbing system. We constrain models of its plumbing system with satellite and airborne interferometric synthetic aperture radar (InSAR) surface displacement observations. Displacement time series from RADARSAT-2 and COSMO-SkyMed satellite data span the entire inflation period from 2011 to 2016, with their initially high rates of 12 and 15 cm/yr, respectively, slowing only slightly through 2016. InSAR observations for the 2013–2016 time period constrain a two-source compound dislocation model, with a rate of volume increase of 13×10^6 m^3/yr. They consist of a shallow, near-vertical, elongated source centered at 2.5 km beneath the summit, and a deeper, shallowly plunging source centered at 7 km depth connecting the shallow source to the deeper caldera. The deeper source is located directly beneath the volcano tectonic seismicity with the lower bounds of the seismicity parallel to the plunge of the deep source. This suggests a deep conduit or transfer zone where magma moves from the central caldera to Copahue's upper edifice.

1. Introduction

Our understanding of volcanic systems and their future behavior depends on interpreting the changes within the volcano's plumbing system as expressed through seismicity, surface deformation, gas, and eruptive emissions. Surface deformation remains one of the major observational controls toward developing numerical physical models of these systems through its constraint on source shape and dimensions, location, depth, and temporal behavior. Over the past two decades interferometric synthetic aperture radar (InSAR), primarily from satellites, has been of fundamental importance for constraining volcano processes with its ability to image surface deformation at meter-scale sampling resolution and subcentimeter precision over broad

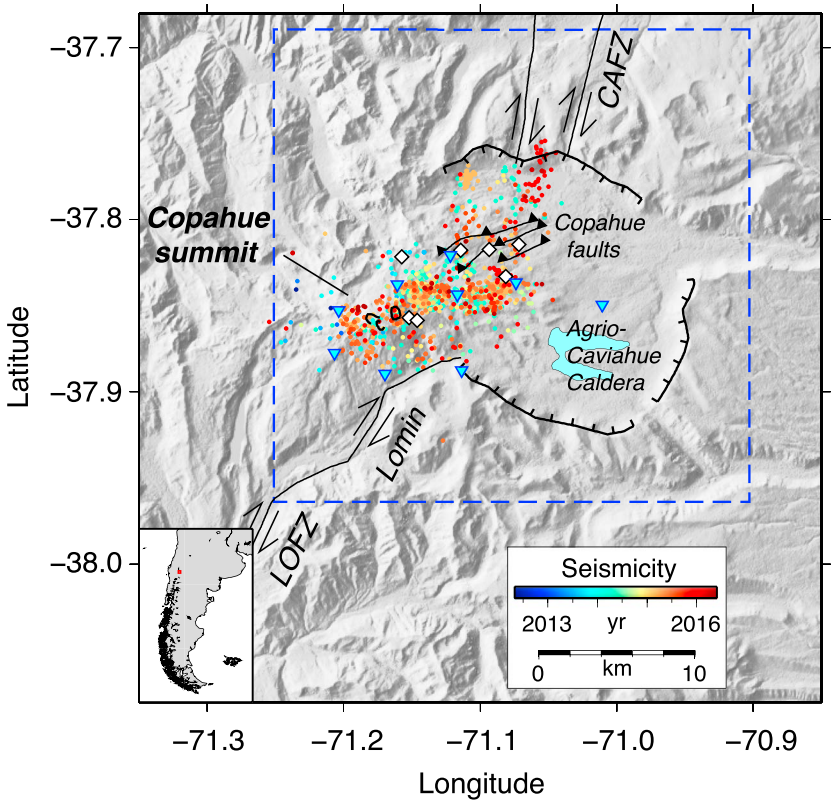

Figure 1. Shaded relief map of Copahue volcano and the adjacent Agrio-Caviahue caldera. Bold lines outline summit craters and lines with tick marks indicate the caldera rim. The right-lateral Liquiñe-Ofqui fault zone (LOFZ), Lomin fault, and the Copahue-Antiñir fault zone (CAFZ) are shown as solid thin lines [*Melnick et al*., 2006; *Bonali et al*., 2016; *Folguera et al*., 2016]. The Copahue faults are shown as solid lines with solid triangular barbs on the hanging walls, considered thrust faults, which in this study we find exhibited normal motion. Volcano tectonic (VT) seismicity for events with location quality ratings of A and B according to the HYPO-71 algorithm [*Lee and Valdes*, 1985] is colored by time. White filled diamonds show the locations of geothermal areas (near the Copahue faults) and hot springs (near Copahue volcano summit) [after *Velez et al*., 2011]. Cyan-filled inverted triangles show locations of seismic stations used in *b* value analysis. Blue dashed box outlines the data area used for modeling.

areas. This has led to numerous insights into hydrothermal activity [*Wicks et al*., 1998; *Lundgren et al*., 2001; *Lundgren and Lu*, 2006; *Chang et al*., 2010], highly dynamic calderas [*Amelung et al*., 2000; *Yun et al*., 2006; *Chang et al*., 2010; *LeMével et al*., 2015], and discoveries of previously unknown magma influx into the crust at locations offset from the nearby active volcano [*Lu et al*., 2002; *Pritchard and Simons*, 2002; *Wicks et al*., 2002; *Fialko and Pearse*, 2012; *Lundgren et al*., 2015]. It is this detailed, yet synoptic view of surface deformation, coupled with satellite InSAR's potential for global reach that has provided important insights into complex volcano source processes beyond simple point sources.

Copahue volcano (Figure 1) (71.16°W, 37.85°S) is a basaltic-andesitic volcano on the Chile-Argentina border in the southern Andes, situated between the intra-arc Liquiñe-Ofqui fault zone (LOFZ) and the Antiñir-Copahue fault zone (ACFZ) [*Folguera et al*., 2004; *Melnick et al*., 2006; *Folguera et al*., 2016]. Copahue lies within the Callaqui-Copahue-Mandolegüe (CCM) volcanic lineament [*Melnick et al*., 2006; *Folguera et al*., 2016], with the NE alignment of Copahue's edifice and summit vents parallel to the direction of maximum compressive stress within the CCM [*Bonali*, 2013]. Its northeast flank is characterized by an alignment of vents and hot springs related to a shallow, seismically active hydrothermal system [*Ibáñez et al*., 2008]. Copahue's high $^{3}He/^{4}He$ and $CO_2/^{3}He$ ratios suggest that it is influenced by its extensional setting, with magmas reflecting mantle asthenospheric upwelling and subducted sediments [*Agusto et al*., 2013]. The high fumarolic gas flux beneath the NE flank of Copahue and the broad area affected are compatible with a large magmatic source beneath this area [*Chiodini et al*., 2015]. This activity has led to extensive hydrothermal alteration, suggesting that edifice flank instability is a potential hazard [*Varekamp et al*., 2001].

During the past 260 years there have been 11 phreatic/phreatomagmatic eruptions, with the most recent ones in 2000 and December 2012–2016 during the current unrest period [*Naranjo and Polanco*, 2004; *Caselli et al*., 2016a, 2016b]. The December 2012 phreatomagmatic-magmatic eruptions (≤VEI 2) were similar to the one in 2000, erupting from the same easternmost summit crater after a period of increasing seismic activity following the 2010 Maule earthquake [*Caselli et al*., 2016b]. Since the 2012 eruptive events, Copahue volcano has developed several episodes of similar phreatomagmatic and magmatic eruptions, with hydrothermal and magmatic systems alternating in dominance, with the most significant occurring during the period between October 2015 and December 2016, when a quasi-continuous Strombolian activity was observed. Numerical modeling of the 2010 Maule earthquake found unclamping of vertical faults that would favor the migration of fluids resulting in the 2011 to present unrest period [*Bonali*, 2013; *Bonali et al*., 2015]. Analysis of pyroclastic density current deposits shows phreatomagmatic vesiculation occurred at 400 m depth with fragmentation occurring through the interaction of magma with a summit hydrothermal system at 1500 m depth beneath the summit [*Balbis et al*., 2016].

In this study, we characterize the sources of inflation at Copahue volcano during an extended period of volcano unrest. We measure surface deformation using synthetic aperture radar (SAR) data from 2011 to 2016. InSAR surface deformation time series velocities are analyzed from ascending and descending track COSMO-SkyMed data and descending track RADARSAT-2 data. We also include, for comparison, airborne UAVSAR data, which provides improved viewing diversity, over a subportion of the unrest period. We apply a new type of analytical solution, the compound dislocation model (CDM) and its point-source version [*Nikkhoo et al*., 2017], to solve for the complex sources constrained by the asymmetric deformation patterns revealed by the InSAR data. We discuss the implications of the source solutions in terms of the volcano plumbing system and eruption processes of the Copahue volcano caldera system.

2. Data Analysis

We used synthetic aperture radar (SAR) data from two satellites and one airborne system: the Canadian Space Agency (CSA) RADARSAT-2 (RSAT2) C-band (5.6 cm wavelength) satellite, the Italian Space Agency (ASI) COSMO-SkyMed (CSK) X-band (3.1 cm wavelength) four-satellite constellation, and the National Aeronautics and Space Administration (NASA) UAVSAR airborne repeat pass interferometry L-band (23.8 cm wavelength) system. For each sensor we compute InSAR maps of relative ground surface deformation projected into the radar line-of-sight (LOS) direction [*Rosen et al*., 2000].

Each sensor's data were processed into differential interferograms, after removal of Earth curvature and topographic effects, with different processing software. For RSAT2 only descending track data were available and were processed at the Canada Centre for Remote Sensing using the Gamma processing package [*Wegmuller and Werner*, 1997]. CSK data were available from both ascending and descending tracks; however, like RSAT2, the CSK background volcano acquisitions are only for descending tracks. Ascending track CSK data were requested beginning in June 2013 once deformation from RSAT2 indicated ongoing inflation. CSK data were processed using the InSAR Scientific Computing Environment (ISCE) package developed at the Jet Propulsion Laboratory (JPL), Caltech, and Stanford University [*Rosen et al*., 2015]. ISCE processing used the SRTM 30 m digital elevation model [*Farr and Rodriguez*, 2007] to correct for topography. For interferogram unwrapping we used the SNAPHU unwrapper [*Chen and Zebker*, 2000] implemented in ISCE. Lists of interferograms used in the analysis are given in the supporting information. Baselines for the CSK data were generally constrained to be within 150 m and 3 months in orbital (perpendicular baselines, $B_{\perp}$) and temporal separation, respectively, but with longer (up to 1.5 years) summer-to-summer pairs required to span winter incoherence. The criteria were similar for the RSAT2 interferograms with $B_{\perp}$ less than 250 m and temporal baselines up to 500 days.

For each satellite data set we compute InSAR time series from sets of interconnected interferograms using the GIAnT software package [*Agram et al*., 2013] in the NSBAS mode. Atmospheric corrections were not applied; instead, to smooth out atmospheric scatter, we used temporal Gaussian filters with lengths of 0.20, 0.05, and 0.10 years for the RSAT2, CSK descending, and CSK ascending solutions, respectively. The filter length depended largely on the temporal sampling, which was sparsest for RSAT2 (with its 24 day repeat orbit) and densest for the CSK descending track (CSK 4 acquisitions possible per 16 days), which had more acquisitions than for the ascending track. The scatter of the raw unfiltered solution (red dots) compared to

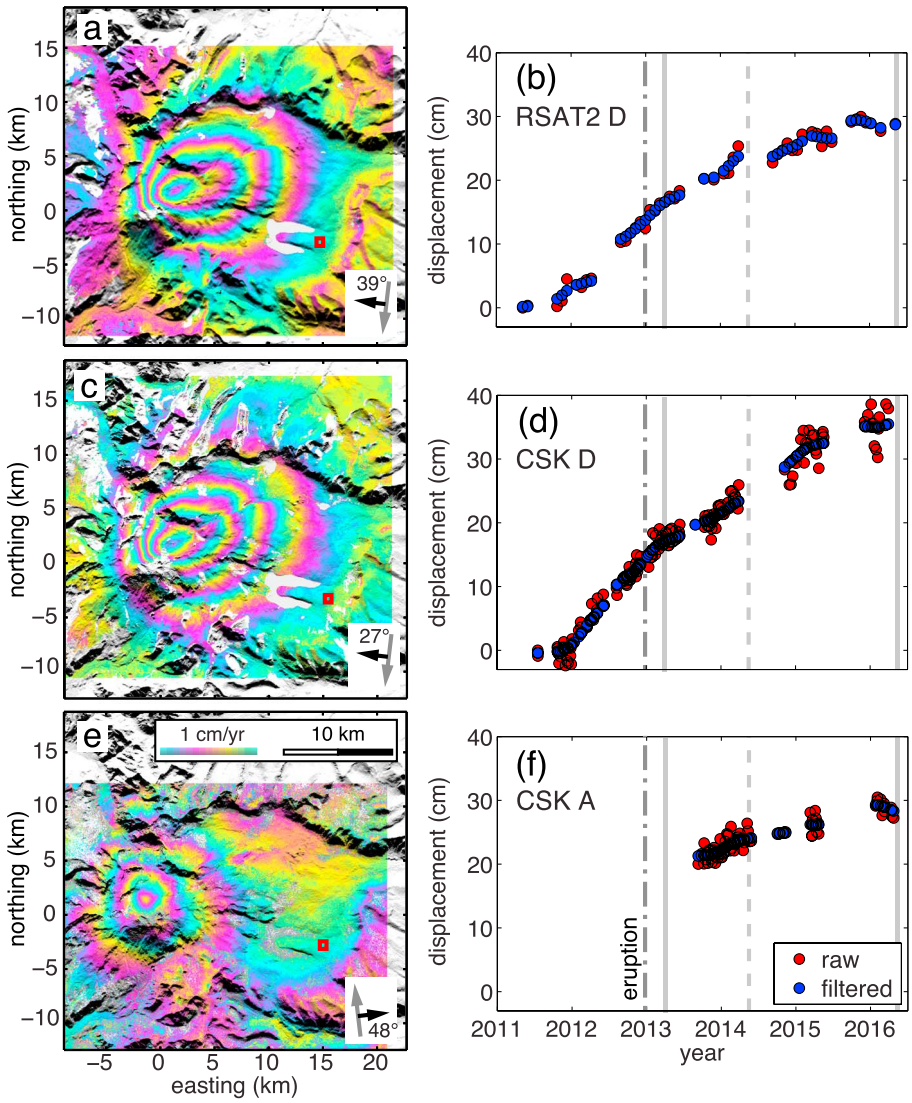

Figure 2. InSAR time series LOS linear velocity maps and peak inflation time series. (a, c, and e) Maps give the linear velocities for the 2013.25–2016.4 interval. The box in the lower right corner of each plot gives the satellite heading direction (gray arrow), the radar look direction (black arrow), and the incidence angle from vertical in degrees. The small red square in each map is the time series reference box (10 × 10 pixels). (b, d, and f) Time series of peak LOS inflation, each corresponding to the map to its left. The scatter of the raw unfiltered solution (red dots) compared to the filtered solution (blue dots) gives a sense of the time series uncertainty. The dark gray dash-dotted line marks the dates of the late phreatomagmatic eruptive period starting in December 2012. The solid gray lines (2013.25–2016.4) mark the limits of the 2013.25–2016.4 linear velocity time window. The solid gray to dashed lines (2013.25–2014.3) mark the dates spanned by the UAVSAR data (and corresponding time series linear velocities).

the filtered solution (blue dots) gives a sense of the time series uncertainty (Figure 2). The InSAR time series show inflation started in late 2011, which was fastest during the initial 3 years, with a slightly lower rate through mid-2016. The start of inflation in late 2011 is also inferred from Envisat time series analysis for the time period 2011.1–2012.25 [*Velez et al.*, 2016]. Due to snow during the austral winter (June through September or October) gaps occur in the time series. The linear (or mean) LOS velocity inflation pattern we find is very distinct, with the descending tracks showing a very similar, elliptical pattern, extending from the summit of Copahue volcano at the SW edge of the caldera toward the ENE interior of the caldera (Figure 2). The descending track data sets provided our initial imaging of the LOS displacements and suggested an asymmetric source directed toward the caldera interior. The ascending track CSK time series show a completely different, roughly circular, pattern centered slightly

north of the summit. Together, the two deformation patterns illustrate the need for both viewing geometries to constrain the source or sources and the importance of having at least two viewing directions (i.e., if you only had the ascending track data its roughly circular pattern might suggest that only a simple Mogi point source solution was required to fit the data).

The UAVSAR interferograms and the satellite InSAR time series linear LOS velocities for the 2013–2014 interval (Table S1) are shown in Figure S1. We show these interferograms along with the time series velocities at a wrap rate of 3 cm/yr. As evident in the UAVSAR interferograms, there is a fair amount of atmospheric or aircraft residual baseline-induced phase noise. In the case of Figure S1e, there was significant topographically correlated noise that we reduced by using a tropospheric phase correction based on the European Centre for Medium-Range Weather Forecasts weather model [*Agram et al*., 2013].

In order to reduce the number of data points to a reasonable number for our Bayesian modeling approach, we downsample interferograms using a model-based quadtree method from *Lohman and Simons* [2005]. A horizontal tensile dislocation model is used to downsample the data to ~500 data points retained, slightly varying for each UAVSAR interferogram or time series linear velocity map. Each downsampled point is computed from the mean value of the original coherent unwrapped phase within each quadtree square area of pixels. Standard deviations (σ) for the points are computed and are generally in the range from 0.1 to 0.3 mm/yr for the linear velocity and 1–2 mm for the interferograms. In our modeling we used the data variances rather than the full data covariances (see section 3) due to computational limitations.

Due to the heterogeneity of the different data sets, we explore two time intervals: the mean velocities from the satellite data for the 2013 through May 2016 period, which gives the longest time series with both descending and ascending data, and the 2013–2014 interval in which we have relatively clean UAVSAR interferograms from three different viewing directions. UAVSAR data were also collected in 2015; however, the quality of the set of three interferograms was poorer than the 2013–2014 interferogram set.

3. Modeling

We use a Bayesian inference approach based on a Markov chain Monte Carlo (MCMC) sampling [*Fukuda and Johnson*, 2010] to estimate posterior probability density functions (PDFs) of model parameters. In our implementation of the MCMC code we run the inversion through one million kept solutions [*Malinverno*, 2002], throwing out the first 100,000 solutions during the "burn-in" phase [*Lundgren et al*., 2015].

Analysis of the InSAR time series from the satellite data shows that over time the pattern of deformation did not change, although there was some reduction in rate, the reason we model time series and interferograms for comparable time intervals. We consider the data from 2013 to the end of summer 2016 (May) to represent the highest-quality data set for modeling. In the supporting information we also show the results for the 2013–2014 interval covered by the UAVSAR data as a basis of comparison to the 2013–2016 time series results.

In initial analyses of the modeled source(s) we used point [*Mogi*, 1958], spheroid [*Yang et al*., 1988], and tensile dislocations [*Okada*, 1985] either alone or in combination. In general, these initial analyses required two sources, one shallower to fit the more acutely shaped deformation source nearer the summit, with a deeper dipping elongated spheroidal and dislocation source required to fit the extended positive line-of-sight (LOS) displacements to the ENE (evident in the descending track while mostly canceling in the ascending track). However, in the case of the spheroidal sources, the large radius of curvature of the deeper source with respect to its depth meant that the Greens functions were inaccurate [*Yang et al*., 1988].

We resolved these previous analytic source limitations by using a new type of analytical source, the compound dislocation model (CDM) and its point-source version, the point-CDM (pCDM) [*Nikkhoo et al*., 2017]. The CDM is composed of three orthogonal tensile dislocations, each with the same opening (or closing) magnitude, giving a total potency, or influx volume ΔV. The CDM has 10 parameters: three for location (x, y, z), three semiaxes lengths (a, b, and c), three axial rotations (ω_x, ω_y, and ω_z), allowing for arbitrary orientation and axes lengths, and uniform opening u. The CDM can approximate shapes ranging from equidimensional, to pancake shaped, to cigar shaped, to pipe like. In the case of the pCDM its

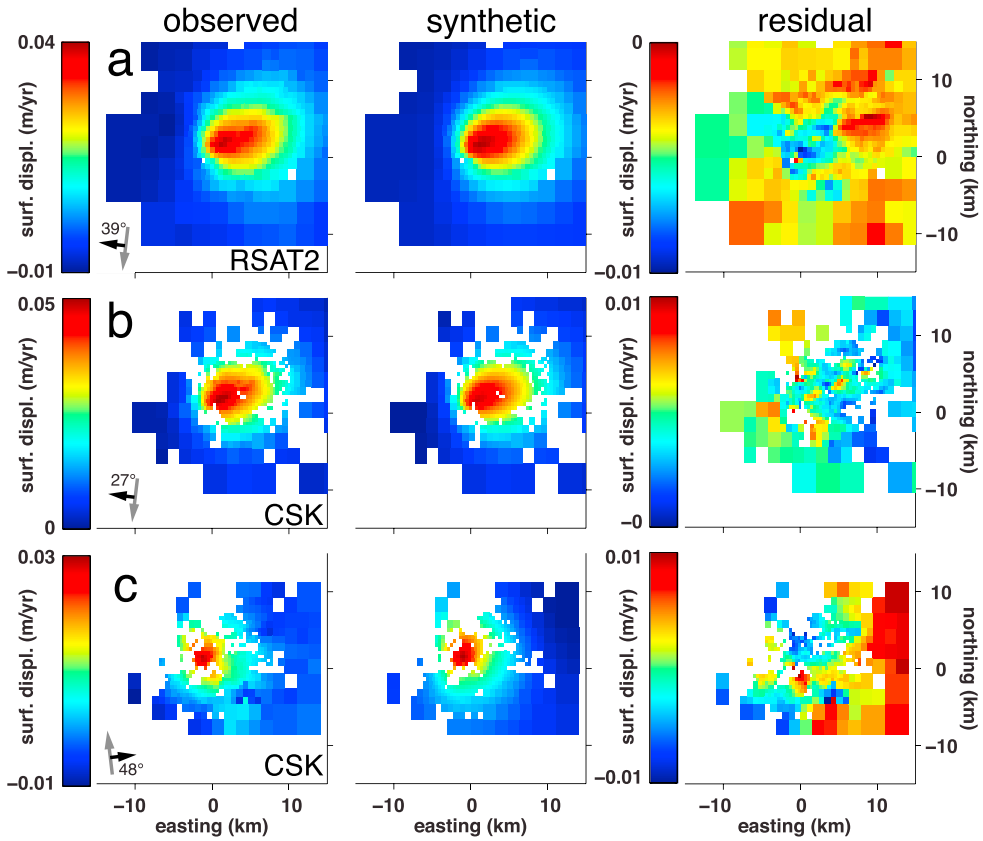

Figure 3. Two source CDM solution modeled InSAR line-of-sight (LOS) surface displacement rates for the 2013.25–2016.4 time interval. For each (left column) observed InSAR time series linear velocity we show the (middle column) synthetic displacements given by the source model and (right column) the residual. For each data set: (a) RSAT2 descending, (b) CSK descending, and (c) CSK ascending track, the satellite heading (gray arrow), look direction (black arrow), and incidence angle are indicated in the lower left corner.

computation time is faster and it has three potencies in place of the axes and uniform opening. For extended sources the pCDM is less accurate than the CDM, but we present it here (and in the supporting information) for comparison and to compare one versus two sources.

The solution for the two CDM source model constrained by the 2013–2016 data set (Figures 3–5 and Table 1) is a very long, thin source located slightly north and several kilometers east of the summit, centered at 7 km depth and plunging shallowly to the ENE. The second source is shallower (2.5 km depth), located above the upper portion of the deep source and elongated steeply toward the summit craters. The rate of influx volume increase (ΔV/yr), or potency rate, is ~13×10^6 m^3/yr, where $\Delta V = 4u(ac + bc + ac)$ and a, b, and c are the semi-axes of the CDM and u is the opening.

We also computed source models using the pCDM solutions for one or two sources (Table 1). The one-source solution results are shown in Figures S2–S4. Results for the two-pCDM solution are shown in Figures S5–S8. The synthetic displacements for the single pCDM appear significantly worse than that for the two-source synthetic, especially for descending track data. We performed an F test of significance (see *Lundgren et al.* [2015] for equation and description). For the pCDM solutions F = 199, which for the large number of data points and the nine additional parameters for the second source, is significant at the 99% confidence level. The pCDM source maps (Figures S4 and S8) show locations and orientations of the three force dipoles for each source that are similar to the potencies or ΔV for the CDM (see *Nikkhoo et al.* [2017] for details). For the pCDMs the potency, ΔV, is simply the sum of the potencies for each axis. The single-source pCDM solution is intermediate in location and mechanism between the two-source solution. As such, it is less able to fit both the shape and extent of the observed LOS displacements. In the case of the two-pCDM source model we can also look at the model parameter

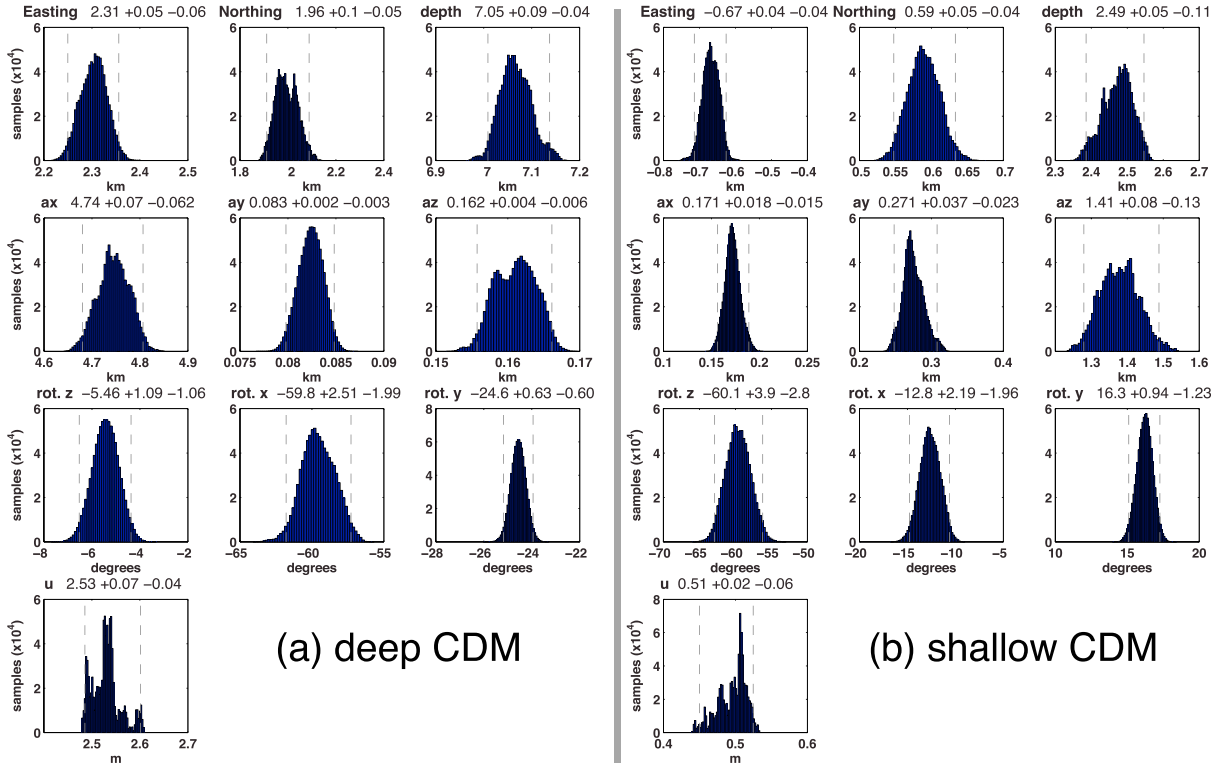

Figure 4. Two source CDM solution posterior probability density functions (PDFs) for each parameter. (a) Deep CDM source. (b) Shallow CDM source. The label for each parameter is given above each subplot. The number adjacent parameter label gives the mode value, and the plus and minus 95% confidence bounds are indicated in the PDF plots by dashed gray lines.

covariances in addition to the PDFs (Figure S7). In general, significant covariance occurs between the ΔVs and the source locations and depths, both within the same source and between sources. Some of these coupled variations in parameters for influx volume and depth are easily understood—the deeper the source the greater the influx volume required to maintain a given magnitude in surface displacement. The coupling between sources is strongest in depth, with opposing covariance in depth—as the deep source moves slightly deeper the shallower one moves toward the surface in compensation. However, it should be noted that the inferred uncertainties in these location parameters are relatively small (0.1–0.2 km in depth and $<$0.1 km in easting and northing; Figure S6).

The root-mean-square (RMS) solution errors are 0.0029, 0.002, and 0.0019 m for the single pCDM, two-source pCDM, two-source CDM solutions, respectively (Table 1). This shows that the CDM solution is about 5% better than the two-source pCDM solution, with the single-source pCDM about 50% poorer in fitting the data. The finite CDM is better able to fit the extended deformation relative to its source depth and the length and orientation of the CDM, not surprising considering the improved fidelity of the CDM solution relative to the pCDM for finite, laterally extended sources [*Nikkhoo et al*., 2017].

We also compare the pCDM results for the UAVSAR data and the InSAR time series for the 2013 to 2014 time interval. We use two pCDMs and find similar results to those for the 2013–2016 InSAR time series linear LOS rates. The model fit to the six InSAR data sets (Figure S9), the PDF distributions (Figure S10), and solution force dipoles (Figure S11) differ mainly in source depths, with the 2013–2014 depths both deeper and shallower compared to the deep and shallow pCDM solutions for the 2013–2016 interval. Because of these shifts, the size for each source in the 2013–2014 interval is larger and smaller for the deep and shallow sources, respectively. These model differences lie beyond their formal uncertainties shown for their distributions (Figures S6 and S10). We interpret these source differences as most likely reflecting data noise due to residual atmospheric effects, rather than true variations in the source locations. Atmospheric effects are particularly significant for the UAVSAR interferograms and can also affect InSAR time series, especially over shorter time intervals. UAVSAR interferograms can also suffer from residual aircraft motion effects.

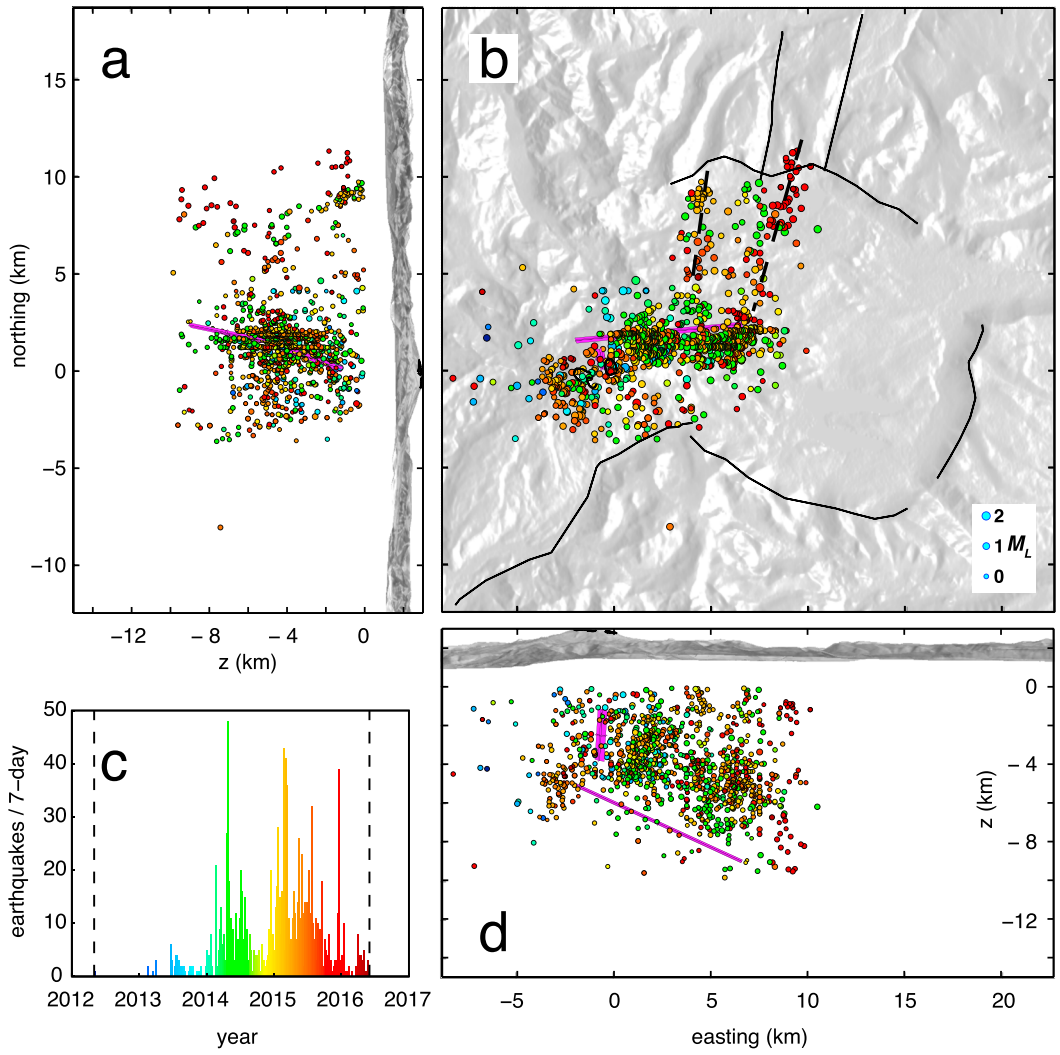

Figure 5. Two-source CDM solutions (magenta) and volcano tectonic (VT) seismicity from the OVDAS catalogue for events with location quality A and B. (a) Side view from the west. (b) Map view, area corresponds to box shown in Figure 1. Dashed black lines north of the sources roughly parallel the two bands of seismicity in the northwest portion of the caldera, similar to the mapped faults (Figure 1) extending to the north of the caldera. (c) Histogram of the number of volcano tectonic (VT) events per week. Color in the histogram and Figures 5a, 5b, and 5d correspond to the date of the earthquake. Seismicity circle size scales with local magnitude (M_L), legend given in Figure 5b.

4. Discussion

There are three interesting aspects to the Copahue source solution that warrant further discussion: (1) the interpretation of the solutions themselves, (2) the comparison of these solutions to other observations from the volcano since the onset of unrest in late 2011, and (3) the relationship of the source to seismicity and eruptive activity.

4.1. Deformation Source Implications

First, the asymmetry in the surface deformation indicates the need for a source extending from the Copahue edifice toward the caldera interior. Given the different viewing geometries of the satellite InSAR data and the apparent asymmetry between the ascending and descending time series linear velocity maps, we consider inverting for the three-dimensional displacements. We performed a least squares inversion of the three InSAR time series for the 2013.25–2016.4 interval up (U), northing (N), and easting (E) components (Figure 6) using the method of *Hu et al.* [2010]. As expected, the N component has very noisy values

Table 1. Source Model Inversion Results[a]

Model (Type N Src Year-Range)	x (km)	y (km)	Depth (km)	a (km)/Pot a (10^6 m^3/yr)	b (km)/Pot b (10^6 m^3/yr)	c (km)/Pot c (10^6 m^3/yr)	ω_X (deg)	ω_Y (deg)	ω_Z (deg)	u (m/yr)	ΔV (10^6 m^3/yr)	RMS (mm/yr)
CDM 2 src 2013–2016	2.31	1.96	7.05	4.74	0.08	0.16	−59.8	−24.6	−5.5	2.53	11.8	1.9
	−0.67	0.59	2.49	0.17	0.27	1.41	−12.8	16.3	−60.1	0.51	1.4	
pCDM 2 src 2013–2016	3.47	2.97	8.44	0.44	2.45	4.71	5.9	−23.4	−16.0	--	7.6	2.0
	−0.90	0.81	4.57	3.64	1.50	0.83	38.7	33.2	−57.6	--	6.0	
pCDM 1 src 2013–2016	−0.85	1.93	7.64	1.43	0.18	9.55	−8.0	−46.6	−27.2	--	11.0	2.9
pCDM 2 src 2013–2014	2.06	0.77	9.0	3.11	3.97	18.1	22.9	−43.1	−32.8	--	25.2	6.0
	−0.36	1.23	2.39	1.34	1.97	0.69	−11.9	−10.5	25.4	--	4.0	

[a]See *Nikkhoo et al.* [2017] for CDM and pCDM definitions.

reflecting the poor constraint on it due to the mostly E-W viewing directions of the SAR satellites, which normally allows for the inversion of only the mostly U + N and E components [e.g., *Lundgren et al.*, 2004; *Milillo et al.*, 2016]. Nonetheless, the U and E components show that there is a significant asymmetry from west to east, with both profiles extending more to the east than to the west of the summit, as expected for an asymmetric source plunging into the caldera to the east (Figure 7a).

It is worth noting that the highly elongated shapes of the two CDMs are outside the moment ratio regimes for pressurized ellipsoidal cavities (from pancakes to cigar-like ellipsoids) as shown in Figure S12 [*Nikkhoo et al.*, 2017]. A more apt comparison might be to the open and closed conduit models of *Bonaccorso and Davis* [1999]. If we compute a very elongated CDM source (Figure S13a), we find that the central dimple in the peak vertical uplift, as well as the horizontal radial displacements, becomes more extreme, more similar to the open conduit model (Figure S13b) than to the closed conduit model (Figure S13c). As the radius of the conduit in Figures S12 and S13 is reduced, the CDM is exactly equivalent to the open conduit case. In our case the deep highly elongated source is shallowly plunging to the ENE, such that the effects of being open or closed may be muted. Nonetheless, the numerical implications of the very elongated source's displacements are that there would be minimal "push" at the "ends" of the source as expected for the closed pipe, but instead, it behaves more like the open pipe solution. Numerically, the very elongated CDM is unable to produce a very elongated closed pipe solution, though as the CDM becomes less extreme it plots in the ellipsoidal regime in Figure S12. In the case of the shallow CDM, assuming its near-vertical orientation as vertical, we find that its vertical and horizontal displacements (Figure S14) lie between those of an open and closed pipe for the same dimensions and depth range.

The deformation data alone cannot provide a unique interpretation of the source model. However, our deformation modeling suggests a few options:

1. Both CDMs represent conduits.
2. For the deep CDM: a network of intersecting dikes and sills, subjected to opening. In this case, they would still have to occupy a rather narrow zone that follows the shallow plunge of the deep CDM. For the shallow CDM: a shallow magma chamber.
3. The deep CDM represents the uppermost part of a large magma body. In this case only the top would yield the observed deformation due to properties of the magma body, such as composition or fluid zonation [*Kazahaya et al.*, 2002]. In contrast, a narrow topped, deeply rooted body under constant change in overpressure would give a distinct deformation signature related to its depth extent that is not evident in the Copahue data, unlike for the case of a broad, shallow sill with a conical deep root [*Yun et al.*, 2006].

4.2. Comparison With Seismicity

It is important to compare the InSAR-constrained solution with observed volcano tectonic (VT) seismicity and volcano activity. We consider unrelocated seismicity from the Southern Andes Volcano Observatory (OVDAS). The OVDAS locations in the catalogue have

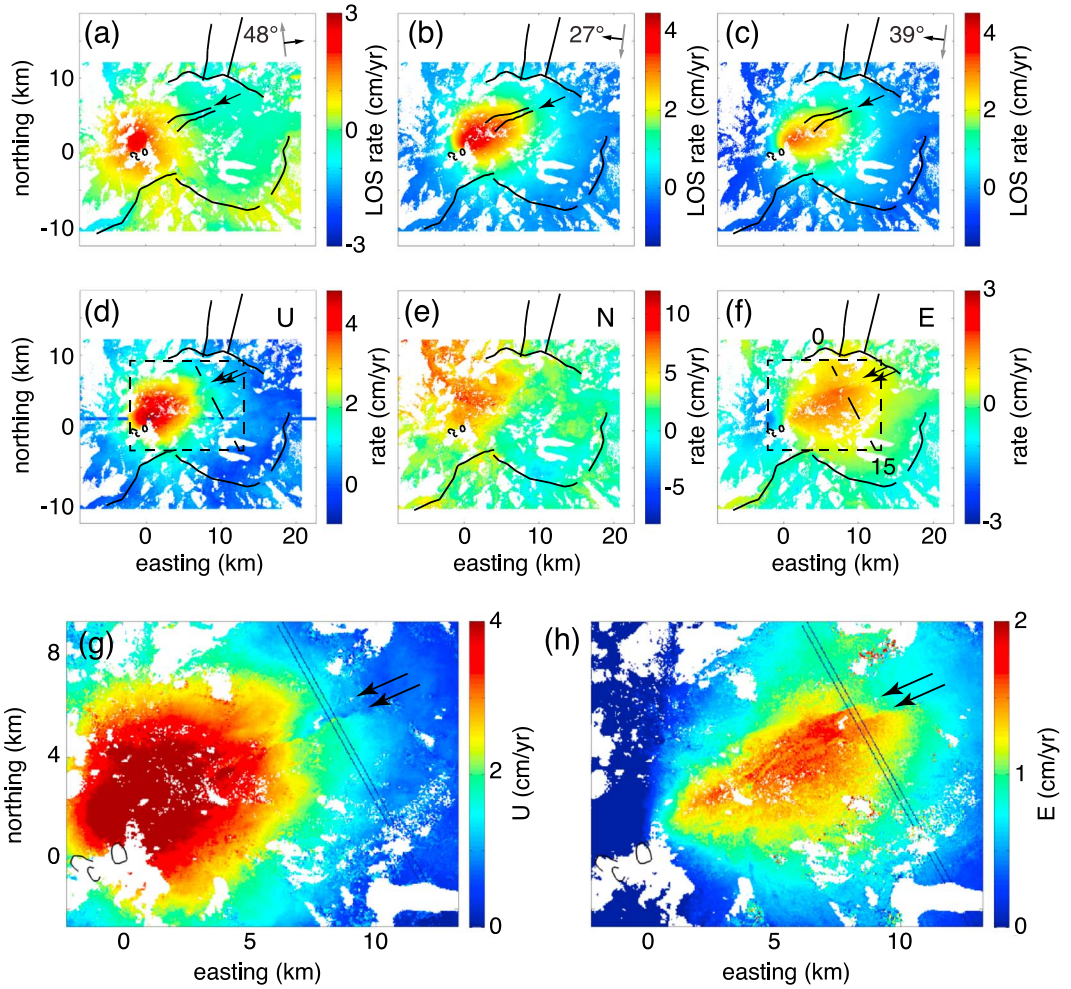

Figure 6. Inversion of InSAR time series linear LOS displacement rates into three-component displacement fields for the 2013–2016 interval. Bold black lines mark faults and caldera boundary, with the summit craters located near the origin. The COSMO-SkyMed (a) (CSK) ascending, the (b) CSK descending, and (c) RADARSAT-2 (RSAT2) descending track data are inverted into the (d) up, (e) north, and (f) east components using the approach of *Hu et al*. [2010]. The blue horizontal 11 pixel-wide stripe in Figure 6d is centered on the profile location shown in Figure 7a. The black arrows in Figures 6d and 6f point to normal faulting discontinuities with the long dashed line marking the profile shown in Figure 7b, and the short dashed box outlines the zoomed in areas shown in Figures 6g and 6h for the up and east rates, respectively. In Figures 6g and 6h the arrows point to the graben-bounding Copahue fault, the two thin parallel lines mark the bounds for the profiles in Figure 7. The two NNW-SSE parallel lines in Figures 6g and 6h show the actual width of the profile (dashed line in Figures 6d and 6f) whose average values along the profile are shown in Figure 7b.

depths relative to zero elevation; however, OVDAS considers the reference elevation at over 3600 m, but this is clearly too high for Copahue, which barely reaches 3000 m, with the low elevation portion of the Agrio-Caviahue caldera below 2000 m. The mean elevation of our InSAR data is 2009 m. In lieu of estimating an exact elevation shift for the solution and the seismicity we simply leave them referenced to zero elevation. We compare the VT OVDAS seismicity with high location quality (A and B) rankings to the CDM two-source model (Figure 5). Comparison of the CDM solutions with the VT seismicity shows an interesting correlation. In map view we see that the seismicity roughly trends along with the deep shallowly plunging source. Viewed from the south, we see that the deep source lies just below and at a similar plunge as the lower bound of the main seismicity cloud. We also find that the shallower source cuts up through the near summit seismicity, although a gap in the seismicity there is unclear. In map view there are two roughly parallel bands of seismicity that extend to the north from roughly the middle and eastern end of the source, likely linked to the Copahue-Antiñir fault zone (CAFZ) [*Melnick et al*., 2006; *Folguera et al*., 2016]. It is worth noting that the eastern extent of the seismicity is within about 2 km of the eastern extent of the

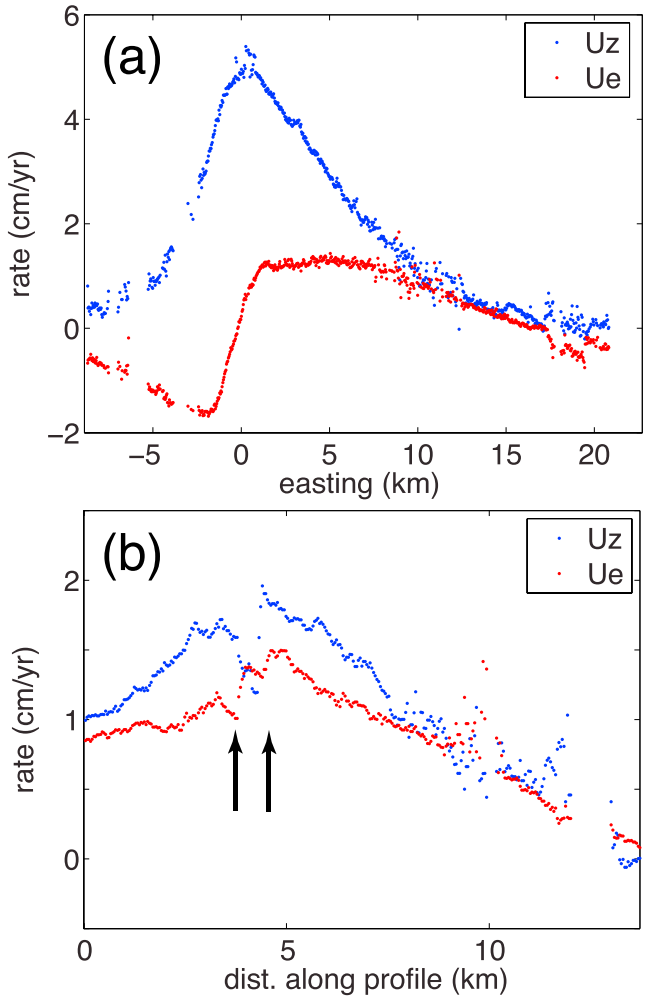

Figure 7. (a) Up (blue) and east (red) component relative motion profiles for the E-W profile location shown in Figure 6d. The asymmetry in both profiles reflects both the two sources and their relative locations and geometries. (b) Up and east displacements along the profile crossing the NE trending faults shown in Figure 6d and 6f by the dashed line.

deep source. Together, these observations suggest that (1) there is a good correspondence between the VT seismicity and the deformation source and (2) the depth and extent of the source and VT seismicity are complementary. For (2) the implication on the depth and trend in depth of the deeper extent of the main VT seismicity cloud is that the deep source lies directly beneath this seismicity. This fits with observations from other volcanoes, such as Mount Etna, where the volcano source forms a "hole" in the VT seismicity, which is concentrated above or to the sides of the source due to higher stress changes surrounding the source [*Patanè et al.*, 2003]. We do not plot the error bars for the seismicity locations; however, the mean standard deviations in the horizontal (1.2 km) and vertical (0.6 km) locations do not significantly affect our inferences regarding their locations relative to the sources.

Also, it is interesting to note that our model matches reasonably well with results on the spatial distribution of the seismicity magnitude-frequency *b* value [*Lazo et al.*, 2015]. Updated *b* value analysis, based on the VT seismic event catalogue from OVDAS for the period December 2012 through September 2016, shows two high *b* value volumes similar to the two CDM sources as well as the locations of active seismic and hydrothermal activity (Figure 8). The spatial *b* value was calculated by means of the *Ishimoto and Iida* [1939] and *Gutenberg and Richter* [1944] methods for magnitude frequency distribution. Using 6172 well-located earthquakes, their spatial distribution was determined with a grid spacing of 100 × 100 m, taking a radius of 1.5 km and a minimum number of 80 events per calculation. Both of the high *b* value regions are related to a production of low magnitude VT events, evidence of regions with more fragile and heterogeneous

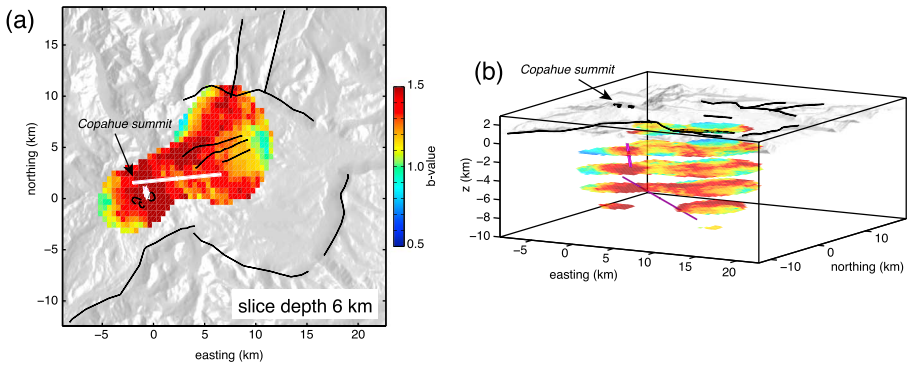

Figure 8. Spatial *b* value variations based on the VT seismic event catalogue from OVDAS for the period December 2012 through September 2016. For reference, we also plot the two-source CDM solution. (a) Plan view for a slice at 6 km depth. Results reveal two high *b* value anomaly zones, one extended zone extending up to 10 km NE from the active crater and a second zone around the active crater (map view). CDM outlines are in white; portion of CDMs shallower than the 6 km slice is colored magenta. (b) Three-dimensional perspective view, from S30°E and 10° elevation angle, of *b* value horizontal slices from 0 to 10 km depth at 2 km intervals. Here we observe the first high *b* value zone (reddish colors) to the NE of the summit spans a depth between 2 and 8 km, while the zone around the crater extends from the surface to 8 km depth. Two-source CDMs are colored magenta with black outlines.

characteristics like hydrothermal and magmatic zones. Analyzing the 3-D distribution, it is possible to observe two possible structures delimited by the high *b* values, one sketching a vertical conduit below the active crater to more than 6 km depth and the other one extending quasi-perpendicular to the first zone below 2 km depth (Figure 8b.). Together, they define an L-shaped structure, reflecting a possible conduit and magmatic reservoir below Copahue volcano. However, there are differences between the spatial distribution of high *b* values and our solutions for two CDMs: (1) the high *b* value structure trending NE from the central conduit below 2 km depth is more aligned with the Copahue faults and the NE flank hydrothermal system, suggesting that it does not reflect the deep deformation source in our model. (2) The high *b* values extending directly beneath the summit craters through at least 6 km depth does coincide roughly with our shallow source. However, it extends deeper than our geodetically determined source, which likely reflects (1) the resolutions of both the geodetic inversion and the *b* value technique in resolving the actual spatial dimensions and (2) that each observation does not correspond to the same process (e.g., the surface deformation is only sensitive to the location of the volume change, whereas the *b* value reflects the broader changes to mechanical properties of the continuum surrounding the sources). This highlights the multiple interpretations for high *b* values, which suggests that some of the higher *b* values to the NE of Copahue's summit may reflect fluid processes in the NE trending Copahue fault zone.

The two parallel bands of VT seismicity to the north of the deep source lie mostly within the caldera, with some events lying north of the caldera between the two main, right-lateral strike-slip faults of the southern CAFZ [*Melnick et al*., 2006; *Folguera et al*., 2016]. Crosscutting this area of the NW caldera is the Copahue fault, a zone of N60°E trending, NW verging thrusts related to the Chancho-Co anticline [*Melnick et al*., 2006; *Bonali et al*., 2016; *Folguera et al*., 2016]. Given the fault complexity within this area of the NW caldera and the apparent northern trends to the seismicity pattern, we compute the Coulomb stress change [*Stein et al*., 1992; *King et al*., 1994; *Toda and Stein*, 2003] for both vertical, N10°E striking, right-lateral strike slip (RLSS) and 60° dipping (to the NW) S60W striking thrust and normal faults (Figure 9). We show the Coulomb stress change (ΔCFS) for depth slices at the near surface (0.25 km depth) and at 5 km depth. For each we show the OVDAS VT seismicity for depth ranges of 0–2.5 km and 2.5–7.5 km. For the RLSS case we see that the north trending bands of seismicity fall within the zone of positive ΔCFS, suggesting promotion of these events within both depth slices (Figures 9a and 9b). The thrust motion on the Copahue fault system would not be promoted at either depth (Figures 9c and 9d). Instead, we see that normal motion would be promoted, although some variation in the pattern would occur with changes in dip angle (Figures 9e and 9f). Regarding the RLSS events, it is also worth noting that the north trending seismicity has only a few events that occur outside the caldera to the north and that these events occur beyond the area with positive ΔCFS, suggesting the extent of positive ΔCFS controls the northern limit to these events. It should also be noted that these ΔCFS computations were carried out assuming a particular effective friction ($\mu' = 0.5$),

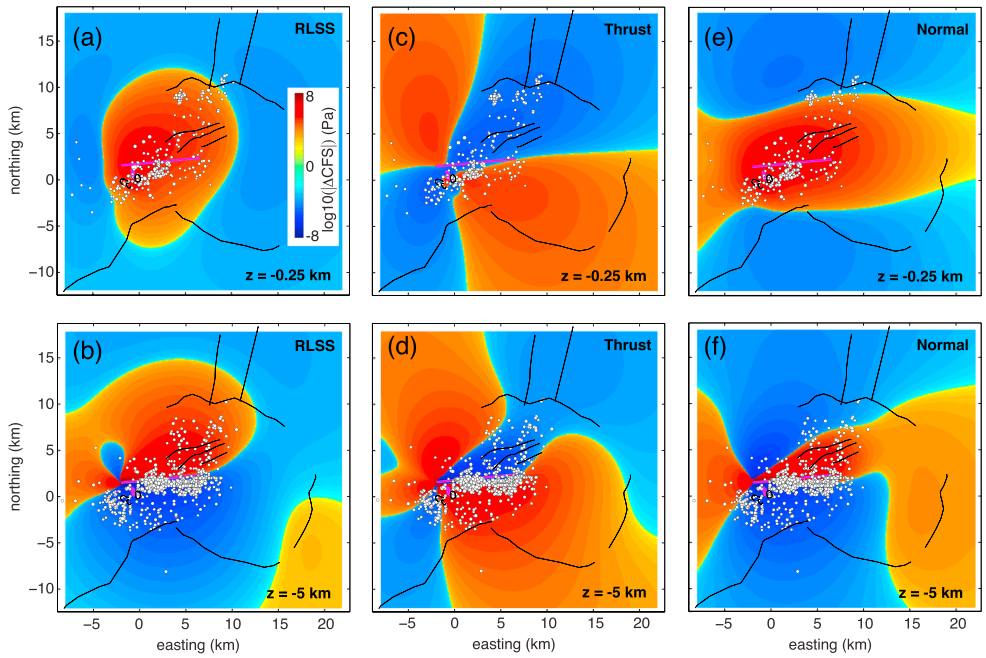

Figure 9. Change in Coulomb fault stress (ΔCFS) for the CDM model (shown in Figure 5) for (a, b) right-lateral vertical strike-slip (RLSS) striking N10°E, for (c, d) S60W striking, 60° dipping thrust faults, and for (e, f) S60 W striking, 60° dipping normal faults. VT seismicity is from the OVDAS catalogue for events with location quality A and B. For plots Figures 9a, 9c, and 9e the ΔCFS is shown at a depth of 0.25 km with seismicity in the depth range from 0 to 2.5 km. For Figures 9b, 9d, and 9f the ΔCFS is for a depth of 5 km with seismicity in the depth range from 2.5 to 7.5 km. The two CDM sources are shown in magenta. For all ΔCFS solutions we use the calc_coulomb function from the Coulomb34 package by S. Toda (toda@rcep.dpri.kyoto-u.ac.jp; https://earthquake.usgs.gov/research/software/coulomb/). We use an effective friction of 0.5 and equal Lamé coefficients of 30 GPa.

receiver fault geometry, and without considering regional stresses, all of which will affect the ΔCFS pattern [*King et al.*, 1994].

The case for normal fault motion derives from the observation in the three-dimensional (3-D) surface displacement rate inversion of fault motion trending to the NE along the NE flank of Copahue (Figure 6). This feature is quite evident in the InSAR time series mean velocities (Figure 2), but it is the decomposition into the 3-D displacements, effectively up and east since the north component is unconstrained that allows us to see there are two parallel faults. These two faults are most evident in the east component (Figure 6f) where the north side moves to the west relative to the south side of each fault. Instead, if we look at the up component (Figure 6d), we see that they constitute a graben, with the area between the two faults subsiding relative to the flanks. In profiles across the structures (black arrows in Figure 7b) we see the downward displaced axial graben and horizontal motion reflecting extension. This fits with the Coulomb stress change calculations (Figures 9e and 9f) showing promotion of normal fault motion. Essentially, this is not surprising since the crust above an inflating body, composed of both vertical and radial horizontal displacements, would promote graben formation and are very similar to structures seen in laboratory experiments for volcano inflation and caldera formation [*Acocella*, 2007].

It is useful to compare our CDM modeling results (Figure 5) to prior InSAR modeling results. *Velez et al.* [2011] studied a period of subsidence from 2002 to 2007 using Envisat SAR data, computing time series LOS mean velocities from both ascending and descending tracks. During this time period they found maximum subsidence rates of nearly 2 cm/yr. Similar to the current episode, the ascending and descending tracks had similar patterns. *Velez et al.* [2011] modeled a single source, comparing solutions for either a Mogi or spheroidal source. Both solutions were located at 4 km depth, with the spheroidal source the preferred solution. *Velez et al.* [2011] interpreted the subsidence and source solution in terms of the release of briny fluids through a sealed carapace, some 3–4 km beneath the summit, at the brittle-plastic transition above a deeper magma body. The depth of the *Velez et al.* [2011] subsidence source is intermediate between our solutions. Since they only modeled a single source in this paper, it is possible there were two sources involved and that their

single-source model solution found a depth intermediate between those for a two-source model. Under that scenario the interpretation might be that both the deep and shallow sources deflated together, thus undermining the sealed carapace interpretation.

More recently, *Velez et al*. [2016] modeled both the 2002–2007 and the 2011–2012 portion of the current unrest, comparing the results for point, spheroidal, and tensile dislocation sources. They found solutions located between 7.5 and 9 km beneath the surface for the current unrest, with the shallower depth found for the point and spheroid sources and the deeper one found for the tensile dislocation (sill) source. *Velez et al*. [2016] preferred the spheroidal source solution since the sill-like dislocation source extended beyond the edifice into the caldera. In order to reduce a positive residual on the volcano's northern flank, *Velez et al*. [2016] added a conduit that they approximated by a high aspect ratio, prolate, inclined spheroid. Their best fit conduit solution was located at 2 km depth beneath the edifice. Conceptually, their two-model solution has similarities with our own: a shallow conduit lying above a deeper source. The main difference between the *Velez et al*. [2016] solution and ours lies in the inclined orientation of our deeper source and the greater depth separation between their sources. It is also worth noting that their volume change (δV), the amount the surrounding medium deforms for a change in pressure within their source volume [see *Nikkhoo et al*., 2017, equation (10)], for the 2011.75–2012.25 (half-year) interval for their two-source solution (δV = 0.050 km^3/yr if assumed a rate) is considerably larger than our two-source pCDM potency change (ΔV) solution (Table S1) for the 2013–2014 interval (ΔV = 0.029 km^3/yr), even though the LOS rates in the ascending tracks were similar (~8 cm/yr). The potency ΔV^E and volume change δV^E of an ellipsoidal cavity are related through $\Delta V^E = \delta V^E + pV/K$, where p is the pressure change and K is the bulk modulus [*Nikkhoo et al*., 2017]. In the case of a Mogi source in a Poisson solid $\Delta V^{\mathrm{Mogi}} = 1.8\delta V^{\mathrm{Mogi}}$, and in the limit of a planar crack $\Delta V = \delta V$ since there is no initial cavity volume V. Therefore, for the same observed deformation the potency of a CDM solution equivalent to a point sphere (Mogi source) should be 1.8 times larger than the volume change derived for the Mogi source. Our problem is the reverse, with $\Delta V < \delta V$, requiring a more fundamental reason for this discrepancy. Some of the differences between their models and ours may be due to their more restricted time interval and having only ascending track data, which likely restricts their model resolution. We also point out that during 2012 we find LOS rates for the descending track time series of approximately 12 and 15 cm/yr for RSAT2 and CSK, respectively. This would imply higher rates of volume change prior to the December 2012 eruptions, which would likely reduce this discrepancy.

Our modeling of the current inflation episode involves both a shallow conduit-like source and a second deeper source. The VT seismicity, despite limitations in location precision (standard deviations of 1.2 km in horizontal and 0.6 km in depth locations) and accuracy due to uncertainties in the velocity structure and reference depth, suggests that the hypocenters are located in close proximity above the modeled sources. Taken at face value, the dimensions and aspect ratio of the deep CDM are unexpected. Numerically, the MCMC solution is allowed to blindly find the best fitting set of two sources to fit the data. In its most literal interpretation the modeled deep source would represent an open pipe, although the CDM solution does not produce a very elongated closed pipe model, and its shallowly reclined orientation means that the deformation is relatively insensitive to it being open. It would represent an inclined conduit, some 160–320 m in diameter and 9 km long. This source appears to connect the shallow near-summit magma body with a deeper source that did not produce resolvable deformation during the study period. However, as mentioned at the end of section 4.1, there are other plausible interpretations either in terms of an inclined plexus of intersecting dikes and sills or the upper extent of a deeper magma reservoir whose primary body does not produce resolvable deformation (Figure 10). It is worth noting at this point that although our interpretation is but one scenario (Figure 10) the highly elongated shape and orientation of the deeper source, pointing from beneath the shallower source toward the center of the caldera, favors a zone of magma transfer (and volume change) from a central caldera source. The lack of a detectable geodetic signature from this deeper caldera source implies that its volume change during this time interval was insignificant relative to its depth, although other volcanoes in the central and northern Andes have produced detectable deformation from deeper sources [*Pritchard and Simons*, 2002; *Fialko and Pearse*, 2012; *Pearse and Lundgren*, 2013; *Remy et al*., 2014; *Lundgren et al*., 2015].

The shallower source, though less elongated, falls outside the ellipsoidal cavity regime in the moment ratio plot (Figure S12). We model the deformation as resulting from two sources; however, the proximity of the

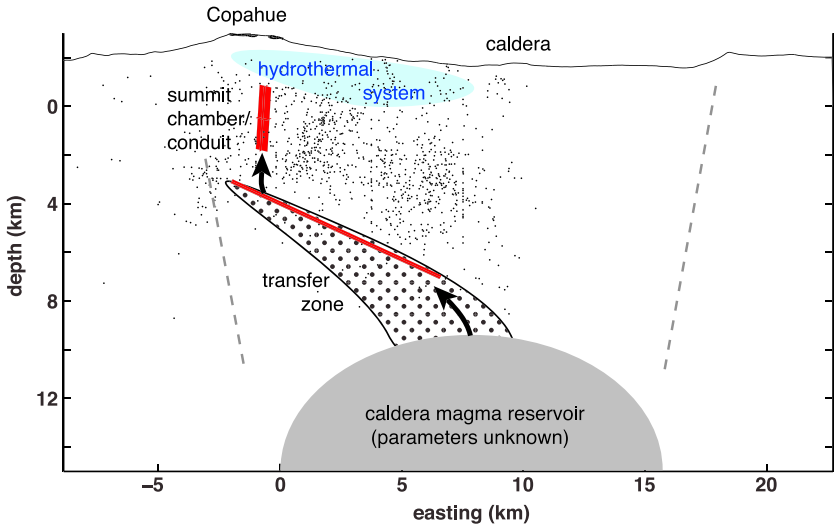

Figure 10. Conceptual diagram for the Copahue volcano-Agrio-Caviahue caldera system. The view is from the south. In red are the modeled CDM solutions; black dots are the OVDAS VT seismicity. Topography profile crosses the summit of Copahue. Dashed lines mark nominal caldera bounding faults; locations and dips are speculative. The eastern end of the deep CDM source suggests that it acts as a zone of magma transfer from a source beneath the center of the caldera, whose depth and size are unknown (gray semiellipse). At shallower depths from the summit of Copahue to the NE lies a hydrothermal system. The stippled region extending from the deep source to beneath the deep CDM source represents the transfer zone of uncertain dimensions.

lower end of the shallow source with the shallower portion of the deeper source suggests that they might represent a single source with a more complex geometry or, at least, two sources that are well connected. This high connectivity is supported by the constant shape of the surface deformation with time.

The rate of influx volume for the CDM and pCDM sources is fairly similar. For the 2013–2016 time interval the influx volume rates are 13.2, 13.2, and $11.0 \times 10^6 m^3$/yr for the CDM two-source, pCDM two-source, and pCDM one-source, respectively. The somewhat smaller ΔV for the single pCDM solution reflects its inability to fit well all the observations and the resultant higher misfit. For the 2013–2014 interval the rate of influx volume ($29.3 \times 10^6 m^3$/yr) is more than double that for the 2013–2016 interval, which reflects the higher deformation rate in the first 2 years of unrest.

Although no quantitative assessments of erupted volume are found for the 2012–2016 eruptions, the assessment of volcanic explosivity index (VEI) 2 eruptions in late December 2012 [*Caselli et al*., 2016b] corresponds to ejecta volumes greater than $1–10 \times 10^6$ m^3, based on the scaling relationship built into the VEI scale [*Newhall and Self*, 1982]. Following the 2012 eruptions, we see only a slight reduction in the inflation rate, suggesting that these small eruptions did not significantly reduce the accumulated pressure increase within Copahue's magmatic system. In fact, as mentioned before, more eruptive episodes occurred through 2016 (OVDAS reports).

4.3. Comparison With Summit Activity

Copahue volcano is an interesting case of ongoing inflation accompanied by eruptive activity. As we have already seen for the VT seismicity (Figure 5c), it starts soon after the start of inflation, with increasing numbers of events through 2015–2016. Previous studies have associated the activity to a delayed response following the 2010 Maule (M_w 8.8) earthquake that would have caused unclamping of the main north and NE oriented vertical faults at Copahue and promoted fluid migration into the volcano from depth [*Bonali*, 2013]. High-quality location VT seismicity at Copahue is not at resolvable numbers in Figure 5c until 2013, after the December 2012 eruption, with the largest numbers of earthquakes reaching maxima in 2014 and 2015, before starting the longest and last eruptive episode characterized by quasi-continuous strombolian activity. Since roughly half of the surface deformation occurred after 2012, this might suggest that VT events were stimulated by increasing Coulomb stress changes due to movement of new magma toward the surface.

The inflation time series, which is characterized either as piecewise linear or as an exponential decay (Figure 2), might result from different mechanisms [*Dzurisin et al*., 2009]. In the absence of eruptive activity (i.e., pressure release), exponentially decreasing inflation rates can be explained conceptually by (1) a hydraulically coupled system of deep and shallow magma reservoirs connected by a conduit [*Reverso et al*., 2014] or (2) viscoelastic relaxation following pressurization of a magma reservoir with a viscoelastic shell [*Dragoni and Magnanensi*, 1989; *Newman et al*., 2001, 2006]. Hydrothermal system models can also exhibit time-dependent behavior due to a pulse of heating at the base of the system, possibly leading to very large displacements for caldera systems such as Campi Flegrei, Italy [*Gaeta et al*., 1998]. However, the hydrothermal system at Copahue is likely restricted to within 1–2 km depth [*Varekamp et al*., 2009; *Agusto et al*., 2013; *Varekamp et al*., 2016] and would not explain the deformation time series that is dominated by the signal from the deeper source.

Distinguishing between these various mechanisms might be accomplished with microgravity observations, assuming that the deformation source is adequately constrained and that corrections to topography, vertical deformation, groundwater, and magma compressibility [*Rivalta and Segall*, 2008] can be made to estimate mass changes that combined with volume change estimates infer the density of the intrusion [*Battaglia et al*., 1999; *Battaglia and Segall*, 2004; *Battaglia et al*., 2008]. With regard to the hydraulically coupled system (1), there is no geodetically resolved deformation signature for a deeper source. The two-chamber model [*Dvorak and Okamura*, 1987], typically invoked to explain exponentially decreasing inflation following an eruption, [*Lu et al*., 2003], involves pressure balance between the shallow and deep reservoir with consideration of the magma flux into the deep chamber as well as the conduit connecting the deep to shallow chambers [*Reverso et al*., 2014]. In the case of Copahue this could mean that the chamber volume change is either too deep or too low in volume change to produce resolvable deformation with InSAR. It is instructive to look at other systems that might place constraints on the magnitude of volume change and depth permitted. For example, Nevado del Ruiz volcano (NRV) recently experienced inflation from a source located 14 km beneath the surface with a volume change rate of ~40×10^6 m^3/yr, which produced an LOS uplift rate of 3 cm/yr. Our estimate for the Copahue volume change rate is around one third to two thirds that of NRV. Such a LOS rate might be evident in the Agrio-Caviahue caldera; however, at NRV the deformation signal spanned some 30 km, roughly the size of the map area in Figure 2. The lack of any such signal suggests that a more likely interpretation would be that any flux of magma from the deeper to shallower chamber (where shallower means both our modeled sources) would be compensated by influx from below into the deep caldera chamber, a hypothesis we cannot test with the geodetic data alone.

The existence of eruptions in 2012 and continual eruptive episodes, as well as gas emission over the period of this study, implies that Copahue is a partially open system. It is interesting, however, that the VT seismicity rates increased and gas flux remained high [*Carn et al*., 2017] since the phreatomagmatic eruption in December 2012 [*Caselli et al*., 2016a, 2016b]. This might suggest that these processes are related to stress increases as volume changes increased at depth and the movement of new magma batches to the surface, giving rise to increased numbers of VT events, possibly facilitating increased gas flux and new magmatic eruptive episodes.

5. Conclusions

InSAR time series from RSAT2 descending and CSK ascending and descending track data for the 2011–2016 unrest period show an asymmetric inflation pattern that started abruptly in late 2011, grew at roughly constant rate (approximately 12 and 15 cm/yr LOS on the RSAT2 and CSK descending track time series) through the main eruptions in December 2012, followed by slightly lower rates of inflation since. Total accumulated RSAT2 and CSK descending track LOS displacements were ~30 and 36 cm, respectively, over 4 years (2012–2016). During the final year of this study (2016) it is unclear whether inflation slowed or possibly stopped, given the uncertainty in the InSAR time series; however, additional RSAT2 data through early 2017 show that inflation continues. We also examined repeat-pass UAVSAR airborne data in 2013–2015. The best set of interferograms for modeling were for 2013–2014 and show inflation consistent with the satellite time series observations.

We modeled the InSAR time series linear velocity deformation maps from 2013 to 2016 using the compact dislocation model (CDM) and, for comparison, the point CDM (pCDM) of *Nikkhoo et al*. [2017]. This time interval allowed us to use time series mean LOS velocities from three satellite tracks (two descending and one

ascending) in order to provide the best constraint on the sources. We found that a two-source model was required for Copahue and that the CDM gives a slightly improved fit to the data compared to the pCDM two-source solution, with the latter solution giving a significantly better fit to the data compared to the single-source pCDM based on an *F* test. Models using the pCDMs give results with a similar interpretation as the CDM solution. Models for the six InSAR data sets (three satellite and three UAVSAR) that covered the 2013–2014 time interval were computed for the two pCDMs. The results are similar to the two pCDM solution for the 2013–2016 InSAR time series satellite data sets.

The preferred two-source CDM gives an interesting, and somewhat surprising solution. The shallow source is elongated, steeply plunging, and centered at 2.5 km beneath the surface, which can be considered to be the 2000 m average elevation of the InSAR data, as shown in Figure 10, thus placing the shallow source roughly at sea level. The second source is much deeper, centered at 7 km below the surface (5 km below sea level), but with a highly elongated, pipe-like shape plunging 25° to the east, whose shallow end lies beneath the shallow summit source and whose deeper end extends into the center of the caldera. The location and orientation of the deep CDM source fits well with the deeper extent of VT seismicity, suggesting that the seismicity is related to stress changes due to the deep source's volume change, whereas the spatial variation in *b* values are sensitive to both the central conduit as well as processes linked to the NE flank fault and hydrothermal systems. While a literal interpretation of the deep CDM source as a narrow (~160 × 320 m cross section) conduit does not fit with typical geodetically constrained volcano sources, it does suggest that much of the surface deformation during the most recent inflation of Copahue volcano occurred in a narrow transfer region between a deeper, unresolved source beneath the caldera and a shallow reservoir beneath Copahue's summit.

Acknowledgments
We thank Francisco Delgado for important discussion and comments that improved the manuscript. We also thank Matt Pritchard and an anonymous reviewer for their important questions and comments. We thank the Canadian Space Agency for providing RADARSAT-2 data. We thank the Italian Space Agency (AS) for providing COSMO-SkyMed data. COSMO-SkyMed (CSK®) products delivered under an Italian Space Agency (ASI) license is made possible through a collaboration between JPL/Caltech/CIDOT and NASA/ASI and as part of the COSMO-SkyMed Announcement of Opportunity (AO), project 188–190. The seismicity catalogue was provided by the Southern Andes Volcano Observatory (OVDAS) from SERNAGEOMIN. Part of this research was carried out at the Jet Propulsion Laboratory, California Institute of Technology, under a contract with the National Aeronautics and Space Administration. Data used in the InSAR analysis may be obtained through the data repository zenodo.org. Local data for Copahue volcano can be accessed from OVDAS through F. Gil-Cruz. This is a contribution to VOLCAPSE, a research project funded by the European Research Council under the European Union's H2020 Programme/ERC consolidator grant [ERC-CoG 646858].

References

Acocella, V. (2007), Understanding caldera structure and development: An overview of analogue models compared to natural calderas, *Earth Sci. Rev.*, *85*, 125–160, doi:10.1016/j.earscirev.2007.08.004.

Agram, P. S., R. Jolivet, B. Riel, Y. N. Lin, M. Simons, E. Hetland, M.-P. Doin, and C. Lasserre (2013), New radar interferometric time series analysis toolbox released, *Eos Trans. AGU*, *94*(7), 69.

Agusto, M., F. Tassi, A.T. Caselli, O. Vaselli, D. Rouwet, B. Capaccioni, S. Caliro, G. Chiodini, and T. Darrah (2013), Gas geochemistry of the magmatic-hydrothermal fluid reservoir in the Copahue–Caviahue volcanic complex (Argentina), *J. Volcanol. Geotherm. Res.*, *257*, 44–56, doi:10.1016/j.jvolgeores.2013.03.003.

Amelung, F., S. Jonsson, H. Zebker, and P. Segall (2000), Widespread uplift and "trapdoor" faulting on Galapagos volcanoes observed with radar interferometry, *Nature*, *407*, 993–996.

Balbis, C., I. A. Petrinovic, and S. Guzmán (2016), A contribution to the hazards assessment at Copahue volcano (Argentina-Chile) by facies analysis of a recent pyroclastic density current deposit, *J. Volcanol. Geotherm. Res.*, *327*, 288–298, doi:10.1016/j.volgeores.2016.08.009.

Battaglia, M., and P. Segall (2004), The interpretation of gravity changes and crustal deformation in active volcanic areas, *Pure Appl. Geophys.*, *161*, 1453–1467.

Battaglia, M., C. Roberts, P. Segall (1999), Magma intrusion beneath Long Valley caldera confirmed by temporal changes in gravity, *Science*, *285*, 2119–2122.

Battaglia, M., J. Gottsmann, D. Carbone, and J. Fernández (2008), 4D volcano gravimetry, *Geophysics*, *73*, WA3–WA18, doi:10.1190/1.2977792.

Bonali, F. L. (2013), Earthquake-induced static stress change on magma pathway in promoting the 2012 Copahue eruption, *Tectonophysics*, *608*, 127–137, doi:10.1016/j.tecto.2013.10.006.

Bonali, F. L., A. Tibaldi, and C. Corazzato (2015), Sensitivity analysis of earthquake-induced static stress changes on volcanoes: The 2010 M_w 8.8 Chile earthquake, *Geophys. J. Int.*, *201*, 1868–1890, doi:10.1093/gji/ggv122.

Bonali, F. L., C. Corazzato, F. Bellotti, and G. Groppelli (2016), Active tectonics and its interactions with Copahue volcano, in *Copahue Volcano*, *Active Volcanoes of the World*, edited by F. Tassi, O. Vaselli, and A. T. Caselli, pp. 23–45, Springer, Berlin.

Bonaccorso A., and P. M. Davis (1999), Models of ground deformation from vertical volcanic conduits with application to eruptions of Mount St. Helens and Mount Etna, *J. Geophys. Res.*, *104*, 10,531–10,542, doi:10.1029/1999JB900054.

Carn S. A., V. E. Fioletov, C. A. McLinden, N. A. Krotkov (2017), A decade of global volcanic SO_2 emissions measured from space, *Sci. Rep.*, *7*, 1–12, doi:10.1038/srep44095.

Caselli, A. T., M. L. Velez, M. R. Agusto, C. Liccioli, and O. Vaselli (2016a), Prehistoric to historic activity at Copahue volcano, in *Copahue Volcano*, *Active Volcanoes of the World*, edited by F. Tassi, O. Vaselli, and A. T. Caselli, pp. 49–59, Springer, Berlin.

Caselli, A. T., M. Agusto, M. L. Velez, P. Forte, C. Bengoa, R. Daga, J. M. Albite, and B. Capaccioni (2016b), The 2012 eruption, in *Copahue Volcano*, *Active Volcanoes of the World*, edited by F. Tassi, O. Vaselli, and A. T. Caselli, pp. 49–59, Springer, Berlin.

Chang, W.-L., R. B. Smith, J. Farrell, and C. M. Puskas (2010), An extra ordinary episode of Yellowstone caldera uplift, 2004–2010, from GPS and InSAR observations, *Geophys. Res. Lett.*, *37*, L23302, doi:10.1029/2010GL045451.

Chen, C. W., and H. A. Zebker (2000), Network approaches to two-dimensional phase unwrapping: Intractability and two new algorithms, *J. Op. Soc. Am. A Op., Image Sci.*, *17*(3), 401–414, doi:10.1364/JOSAA.17.000401.

Chiodini, G., C. Cardellini, M. C. Lamberti, M. Agusto, A. Caselli, C. Liccioli, G. Tamburello, F. Tassi, O. Vaselli, and S. Caliro (2015), Carbon dioxide diffuse emission and thermal energy release from hydrothermal systems at Copahue–Caviahue volcanic complex (Argentina), *J. Volcanol. Geotherm. Res.*, *304*, 294–303, doi:10.1016/j.volgeores.2015.09.007.

Dragoni, M., and C. Magnanensi (1989), Displacement and stress produced by a pressurized, spherical magma chamber, surrounded by a viscoelastic shell, *Phys. Earth Planet. Inter. 56*, 316–328.

Dvorak, J., and A. T. Okamura (1987), A hydraulic model to explain variations in summit tilt rate at Kilauea and Mauna Loa volcanoes, in volcanism in Hawaii, edited by R. W. Decker, T. L. Wright, and P. H. Stauffer, *US Geol. Surv. Prof. Pap.*, *1350*, 1281–1296.

Dzurisin, D., M. Lisowski, and C. W. Wicks (2009), Continuing inflation at three Sisters volcanic center, central Oregon Cascade range, USA, from GPS, leveling, and InSAR observations, *Bull. Volcanol.*, *71*, 1091–1110, doi:10.1007/s00445-009-0296-4.

Farr, T. G., and E. Rodriguez (2007), The shuttle radar topography mission, *Rev. Geophys.*, *45*, RG2004, doi:10.1029/2005RG000183.

Fialko, Y., and J. Pearse (2012), Sombrero uplift above the Altiplano-Puna magma body: Evidence of a ballooning mid-crustal diaper, *Science*, *338*(6104), 250–252.

Folguera, A., V. A. Ramos, R. L. Hermanns, and J. Naranjo (2004), Neotectonics in the foothills of the southernmost central Andes (37–38°S): Evidence of strike-slip displacement along the Antiñir-Copahue fault zone, *Tectonics*, *23*, TC5008, doi:10.1029/2003TC001533.

Folguera, A., E. Rojas Vera, L. Vélez, J. Tobal, D. Orts, M. Agusto, A. Caselli, and V. A. Ramos (2016), A review of the geology, structural controls, and tectonic setting of Copahue volcano, southern volcanic zone, Andes, Argentina, in *Copahue Volcano*, *Active Volcanoes of the World*, edited by F. Tassi, O. Vaselli, and A. T. Caselli, pp. 3–22, Springer, Berlin.

Fukuda, J., and K. M. Johnson (2010), Mixed linear–non-linear inversion of crustal deformation data: Bayesian inference of model, weighting and regularization parameters, *Geophys. J. Int.*, *181*, 1441–1458, doi:10.1111/j.1365-246X.2010.04564.x.

Gaeta, F. S., G. De Natale, F. Peluso, G. Mastrolorenzo, D. Castagnolo, C. Troise, F. Pingue, D. G. Mita, and S. Rossano (1998), Genesis and evolution of unrest episodes at Campi Flegrei caldera: The role of thermal fluid-dynamical processes in the geothermal system, *J. Geophys. Res.*, *103*, 20,921–20,933, doi:10.1029/97JB03294.

Gutenberg, R. and C.F. Richter (1944). Frequency of earthquakes in California, *Bull. Seismol. Soc. Am.*, *34*, 185–188.

Hu, J., Z.-W. Li, J.-J. Zhu, X.-C. Ren, and X.-L. Ding (2010), Inferring three-dimensional surface displacement field by combining SAR interferometric phase and amplitude information of ascending and descending orbits, *Sci. China Earth Sci.*, *53*, 550–560, doi:10.1007/s11430-010-0023-1.

Ibáñez, J. M., E. Del Pezzo, C. Bengoa, A. Caselli, G. Badi, and J. Almendros (2008), Volcanic tremor and local earthquakes at Copahue volcanic complex, southern Andes, Argentina, *J. Volcanol. Geotherm. Res.*, *174*, 284–294, doi:10.1016/j.jvolgeores.2008.02.005.

Ishimoto, M., and K. Iida (1939), Observations of earthquakes registered with the microseismograph constructed recently, *Bull. Earthquake Res. Inst.*, *17*, 443–478.

Kazahaya, K., H. Shinohara, and G. Saito (2002), Degassing process of Satsuma-Iwojima volcano, Japan: Supply of volatile components from a deep magma chamber, *Earth Planets Space*, *54*, 327–335.

King, G. C. P., R. S. Stein, and J. Lin (1994), Static stress changes and the triggering of earthquakes, *Bull. Seismol. Soc. Am.*, *84*, 935–953.

Lazo, J., D. Basualto, C. Bengoa, C. Cardona, et al. (2015), Spatial distribution of *b*-value of the Copahue volcano during 2012–2014 eruptive period: Relationship between magmatic and hydrothermal system, EGU General Assembly Conf. Abstr., 17, 982.

Lee, W. H. K. and C. M. Valdes (1985), HYP071PC: A personal computer version of the HYPO71 earthquake location program, *U. S. Geol. Surv. Open File Rep. 85–749*, pp. 43.

LeMével, H., K. L. Feigl, L. Córdova, C. DeMets, and P. Lundgren (2015), Evolution of unrest at Laguna del Maule volcanic field (Chile) from InSAR and GPS measurements, 2003 to 2014, *Geophys. Res. Lett.*, *42*, 6590–6598, doi:10.1002/2015GL064665.

Lohman, R. B., and M. Simons (2005), Some thoughts on the use of InSAR data to constrain models of surface deformation: Noise structure and data downsampling, *Geochem. Geophys. Geosyst.*, *6*, Q01007, doi:10.1029/2004GC000841.

Lu, Z., C. Wicks, D. Dzurisin J. Power, S. Moran, and W. Thatcher (2002), Magmatic inflation at a dormant stratovolcano: 1996–98 Activity at Mount Peulik volcano, Alaska, revealed by satellite radar interferometry, *J. Geophys. Res.*, *107*(B7), 2134, doi:10.1029/2001JB000471.

Lu, Z., T. Masterlark, D. Dzurisin, R. Rykhus, and C. Wicks Jr. (2003), Magma supply dynamics at Westdahl volcano, Alaska, modeled from satellite radar interferometry, *J. Geophys. Res.*, *108*(B7), 2354, doi:10.1029/2002JB002311.

Lundgren, P., and Z. Lu (2006), Inflation model of Uzon caldera, Kamchatka, constrained by satellite radar interferometry observations, *Geophys. Res. Lett.*, *33*, L063012, doi:10.1029/2005GL025181.

Lundgren, P., S. Usai, E. Sansosti, R. Lanari, M. Tesauro, G Fornaro, and P. Berardino (2001), Modeling surface deformation observed with synthetic aperture radar interferometry at Campi Flegrei caldera, *J. Geophys. Res.*, *106*, 19,355–19,366, doi:10.1029/2001JB000194.

Lundgren, P., F. Casu, M. Manzo, A. Pepe, P. Berardino, E. Sansosti, and R. Lanari (2004), Gravity and magma spreading of Mount Etna volcano revealed by radar interferometry, *Geophys. Res. Lett.*, *31*, L04602, doi:10.1029/2003GL018736.

Lundgren, P., S. V. Samsonov, C. M. López Velez, and M. Ordoñez (2015), Deep source model for Nevado del Ruiz volcano, Colombia, constrained by interferometric synthetic aperture radar observations, *Geophys. Res. Lett.*, *42*, 4816–4823, doi:10.1002/2015GL063858.

Malinverno, A. (2002), Parsimonious Bayesian Markov chain Monte Carlo inversion in a nonlinear geophysical problem, *Geophys. J. Int.*, *151*, 675–688.

Melnick, D., A. Folguera, and V. A. Ramos (2006), Structural control on arc volcanism: The Caviahue-Copahue complex, central to Patagonian Andes transition (38°S), *J. S. Am. Earth Sci.*, *22*, 66–88, doi:10.1016/j.jsames.2006.08.008.

Milillo, P., R. Bürgmann, P. Lundgren, J. Salzer, D. Perissin, E. Fielding, F. Biondi, and G. Milillo (2016). Space geodetic monitoring of engineered structures: The ongoing destabilization of the Mosul dam, Iraq, *Sci. Rep.*, *6*, 37408, doi:10.1038/srep37408.

Mogi, K. (1958), Relations between the eruptions of various volcanoes and the deformations of the ground surfaces around them, *Bull. Earthquake Res. Inst., Tokyo*, *36*, 99–134.

Naranjo, J. A., and E. Polanco (2004), The 2000 AD eruption of Copahue volcano, southern Andes, *Rev. Geol. Chile*, *31*, 279–292, doi:10.4067/S0716-02082004000200007.

Newhall, C. G., and S. Self (1982), The volcanic explosivity index (VEI): An estimate of explosive magnitude for historical volcanism, *J. Geophys. Res.*, *87*, 1231–1238, doi:10.1029/JC087iC02p01231.

Newman, A. V., T. H. Dixon, G. Ofoegbu, and J. E. Dixon (2001), Geodetic and seismic constraints on recent activity at Long Valley caldera, California: Evidence for viscoelastic rheology, *J. Volcanol. Geotherm. Res. 105*, 183–206.

Newman, A. V., T. H. Dixon, and N. Gourmelen (2006), A four-dimensional viscoelastic deformation model for Long Valley Caldera, California, between 1995 and 2000, *J. Volcanol. Geotherm. Res. 15*, 244–269, doi:10.1016/j.jvolgeores.2005.07.017.

Nikkhoo, M., T. R. Walter, P. R. Lundgren, and P. Prats-Iraola (2017), Compound dislocation models (CDMs) for volcano deformation analysis, *Geophys. J. Int.*, *208*, 877–894, doi:10.1093/gji/ggw427.

Okada, Y. (1985), Surface deformation due to shear and tensile faults in a half-space, *Bull. Seismol. Soc. Am.*, *75*, 1135–1154.

Patanè, D., P. De Gori, C. Chiarabba, and A. Bonaccorso (2003), Magma ascent and the pressurization of Mount Etna's volcanic system, *Science*, *299*, 2061–2064, doi:10.1126/science.1080653.

Pearse, J., and P. Lundgren (2013), Source model of deformation at Lazufre volcanic center, central Andes, constrained by InSAR time series, *Geophys. Res. Lett.*, *40*, 1059–1064, doi:10.1002/grl.50276.

Pritchard, M. E., and M. Simons (2002), A satellite geodetic survey of large-scale deformation of volcanic centres in the central Andes, *Nature*, *418*, 167–171.

Remy, D., J. L. Froger, H. Perfettini, S. Bonvalot, G. Gabalda, F. Albino, V. Cayol, D. Legrand, and M. Saint Blanquat (2014), Persistent uplift of the Lazufre volcanic complex (Central Andes): New insights from PCAIM inversion of InSAR time series and GPS data, *Geochem. Geophys. Geosyst.*, *15*, 3591–3611, doi:10.1002/2014GC005370.

Reverso, T., J. Vandemeulebrouck, F. Jouanne, V. Pinel, T. Villemin, E. Sturkell, and P. Bascou (2014), A two-magma chamber model as a source of deformation at Grímsvötn volcano, Iceland, *J. Geophys. Res. Solid Earth*, *119*, 4666–4683, doi:10.1002/2013JB010569.

Rivalta, E., and P. Segall (2008), Magma compressibility and the missing source for some dike intrusions, *Geophys. Res. Lett.*, *35*, L04306, doi:10.1029/2007GL032521.

Rosen, P. A., S. Hensley, I. R. Joughin, F. K. Li, S. N. Madsen, E. Rodriguez, and R. M. Goldstein (2000), Synthetic aperture radar interferometry, *Proc. IEEE*, *88*, 333–382.

Rosen, P. A., E. M. Gurrola, P. S. Agram, G. F. Sacco, and M. Lavalle (2015), The InSAR Scientific Computing Environment (ISCE): A python framework for Earth science, Abstract IN11C-1789 presented at 2015 Fall Meeting, AGU, San Francisco, Calif.

Stein, R. S., G. C. P. King, and J. Lin (1992), Change in failure stress on the southern San Andreas Fault system caused by the 1992 magnitude = 7.4 Landers earthquake, *Science*, *258*, 1328–1332.

Toda, S., and R. Stein (2003), Toggling of seismicity by the 1997 Kagoshima earthquake couplet: A demonstration of time-dependent stress transfer, *J. Geophys. Res.*, *108*(B12), 2567, doi:10.1029/2003JB002527.

Varekamp, J. C., A. P. Ouimette, S. W. Herman, A. Bermúdez, and D. Delpino (2001), Hydrothermal element fluxes from Copahue, Argentina: A "beehive" volcano in turmoil, *Geology*, *29*, 1059–1062, doi:10.1130/0091-7613(2001)029.

Varekamp, J. C., A. P. Ouimette, S. W. Herman, K. S. Flynn, A. Bermúdez, and D. Delpino (2009), Naturally acid waters from Copahue volcano, Argentina, *Appl. Geochem.*, *24*, 208–220, doi:10.1016/j.apgeochem.2008.11.018.

Varekamp, J. C., J. E. Zareski, L. M. Camfield, and E. Todd (2016), Copahue volcano and its regional setting, in *Copahue Volcano*, *Active Volcanoes of the World*, edited by F. Tassi, O. Vaselli, and A. T. Caselli, pp. 81–117, Springer, Berlin.

Velez, M. L., P. Euillades, A. Caselli, M. Blanco, J. M. Díaz (2011), Deformation of Copahue volcano: Inversion of InSAR data using a genetic algorithm, *J. Volcanol. Geotherm. Res.*, *202*, 117–126, doi:10.1016/j.jvolgeores.2011.01.012.

Velez, M. L., P. Euillades, M. Blanco, and L. Euillades (2016), Ground deformation between 2002 and 2013 from InSAR observations, in *Copahue Volcano*, *Active Volcanoes of the World*, edited by F. Tassi, O. Vaselli, and A. T. Caselli, pp. 175–198, Springer, Berlin.

Wegmuller, U., and C. Werner (1997), Gamma SAR processor and interferometry software: The 3rd ERS symposium on space at the service of our environment, Florence, Italy.

Wicks, C., W. Thatcher, and D. Dzurisin (1998), Migration of fluids beneath Yellowstone caldera inferred from satellite radar interferometry, *Science*, *282*, 458–462.

Wicks, C., D. Dzurisin, S. Ingebritsen, W. Thatcher, Z. Lu, and J. Iverson (2002), Magma intrusion beneath the Three Sisters volcanic center in the Cascade Range of Oregon, USA, from interferometric radar measurements, *Geophys. Res. Lett.*, *29*(7), doi:10.1029/2001GL014205.

Yang, X.-M., P. Davis, and J. H. Dieterich (1988), Deformation from inflation of a dipping finite prolate spheroid in an elastic half-space as a model for volcanic stressing, *J. Geophys. Res.*, *93*, 4249–5257, doi:10.1029/JB093iB05p04249.

Yun, S., P. Segall, and H. Zebker (2006), Constraints on magma chamber geometry at Sierra Negra volcano, Galapagos Islands, based on InSAR observations, *J. Volcanol. Geotherm. Res.*, *150*(1–3), 232–243.